plasma

MDPI

Article

Effect of Dielectric Thickness on Filamentary Mode Nanosecond-Pulse Dielectric Barrier Discharge at Low Pressure

Anbang Sun [1,*], Yulin Guo [1], Yanru Li [2] and Yifei Zhu [1]

[1] State Key Laboratory of Electrical Insulation and Power Equipment, School of Electrical Engineering, Xi'an Jiaotong University, Xi'an 710049, China; guoyulin@stu.xjtu.edu.cn (Y.G.)
[2] State Grid Gansu Electric Power Company Electric Power Research Institute, Lanzhou 730070, China
* Correspondence: anbang.sun@xjtu.edu.cn

Abstract

Filamentary mode, as a common phenomenon that appears in dielectric barrier discharge (DBD), is realized by rod-to-rod electrodes in N_2-O_2 mixtures at 80 mbar. The effects of the dielectric thickness on the characteristics of filamentary DBD are investigated through experiments and simulations. The discharges are driven by a positive unipolar nanosecond pulse voltage with 15.8 kV amplitude, 9 ns rise time ($T_r^{10–90\%}$), and 14 ns pulse width. The characteristics of filamentary DBD are recorded with an intensified charge-coupled device and a Pearson current probe in the experiment, and a 2D axisymmetric fluid mode is established to analyze the discharge. Surface discharges occur on the anode and cathode dielectric after the breakdown, and the discharge is gradually extinguished as the applied voltage decreases. A thinner total dielectric thickness ($D_a + D_c$) leads to larger currents, stronger discharges, and wider discharge channels. These characteristics are consistent when the total dielectric thickness is the same but anode dielectric thickness and cathode dielectric thickness are different ($D_a \neq D_c \neq 0$). If the anode is a metal electrode ($D_a = 0$), the current will be substantially large, and two discharge modes are observed: stable mono-filament discharge mode and random multi-filament discharge mode. It is found in simulations that the dielectric thickness changes the electric field configuration. The electric field is stronger with the decrease in dielectric thickness and leads to a more intense ionization which is responsible for most of the observed effects.

Keywords: fluid model; dielectric barrier discharge; streamer

Check for updates

Academic Editor: Andrey Starikovskiy

Received: 19 December 2025
Revised: 25 January 2026
Accepted: 26 January 2026
Published: 27 January 2026

Copyright: © 2026 by the authors. Licensee MDPI, Basel, Switzerland. This article is an open access article distributed under the terms and conditions of the Creative Commons Attribution (CC BY) license.

1. Introduction

Dielectric barrier discharge (DBD) is a typical source of low-temperature plasmas, and provides high-energy electrons and active species at low gas temperatures. DBD has two discharge morphologies which are filamentary mode and diffuse mode. Diffusion mode discharge is more homogeneous and it follows the Townsend discharge or glow discharge mechanism, and filamentary mode follows the streamer discharge mechanism and each filament can be viewed as a separate plasma reactor. Traditional dielectric barrier discharge has a wide range of applications [1–4]; in some cases, filamentary discharge is more efficient, as in the surface modification of special geometric materials [5], targeted therapy in biomedicine [6,7], and the mechanism explanation of partial discharge [8].

The properties of filamentary discharge have been studied through experiments [9–18] and simulations [19–23]. In experiments, N Sewraj et al. used small plane-parallel double barrier configuration electrodes to ignite filamentary DBDs at 50 torr and 760 torr. The

formation of filamentary discharge has three stages: electronic avalanche, cathode-directed streamer and the cathode layer formation [15]. In addition, they calculated the energy and charge injected in a single discharge in the atmosphere which were determined to be (157.9 ± 2.0) μJ and (17.72 ± 0.22) nC, respectively [16]. R Brandenburg et al. developed a special type of DBD arrangement that is two semi-spherical electrodes with a glass covering [17]; they photographed the discharge in the axial and radial directions and the results showed the discharge channel is wider near the electrode because the surface discharge propagates outwards from the volume discharge axis; furthermore, a branched structure was observed not only on the cathode but on the anode [18]. In simulation, the fluid model is widely used. Papageorghiou et al. established a plane-parallel electrode model and their results showed the role of photoemission can be negligible in the formation and propagation of surface discharge in N_2; in addition, the conductivity is large and the voltage drop is small in the discharge channel [20]. The streamer–surface interaction in Ar was explored by Aleksandar P Jovanovic et al. [23]; the discharge was performed in rod-to-rod electrodes in which the cathode is covered with a dielectric. Volume streamer deflection and surface streamer were observed on the dielectric surface, the former was caused by the strong radial component of the electric field, and the latter was caused by secondary electron emission and the accumulation of surface charges.

The shape of the applied voltage is an essential factor in the generation of DBD. The nanosecond pulsed discharge has received attention over the past decade [24,25], compared with sinusoidally driven discharges, it can produce higher energy electrons with less energy loss, is beneficial to ionization, dissociation, and excitation, and can improve the conversion efficiency of active species. In traditional plane-parallel electrodes, nanosecond pulses are more helpful in generating homogeneous DBD [26,27], but in some special electrode configurations, the filamentary discharge is generated. Shuhai Liu et al. used the knife–plate electrode and the applied pulse voltage had a rise time of 14 ns [28]. Thirty-two streamers were generated from a 25 mm knife electrode, and a second discharge occurred at the falling slope. Furthermore, the results show that the initial discharge voltage is about three times the DC breakdown voltage. H Höft et al. performed experiments in rod-to-rod electrodes, the pulse voltage had a rise time of 75 ns [29]. The streak and ICCD images were taken and the discharge development over time was analyzed, they found the discharge had a transient glow phase after the streamer reached the cathode and the discharge diameter near the anode was larger for electrons as the main carriers which move towards the anode in a few nanoseconds [29]. They also investigated the effect of voltage slope steepness between 75 $V{\cdot}ns^{-1}$ and 200 $V{\cdot}ns^{-1}$ [30], the steeper voltage slopes lead to larger electrical currents, more transferred charge, and higher electrical energy.

The dielectric layer is very important in DBD, and typical dielectric materials are alumina, quartz glass, and polymers. The properties of the dielectric affect the characteristics of dielectric barrier discharge. It is commonly known that charge deposition on the dielectric surface creates a space charge field that weakens the applied electric field in the gas gap, causing the discharge to extinguish [31]. Gibalov et al. found the ratio (ε_r/d) of the relative permittivity ε_r to the thickness of the dielectric layer d determines the charge transferred in the discharge [32]. A Ozkan et al. used a specially constructed electrode to convert CO_2, and the CO_2 conversion increases by 50% when the dielectric thickness increases from 2 mm to 2.8 mm [33]. Annette Meiners et al. systematically studied the effect of dielectric properties on discharge efficiency [34]. The results showed that the density of electron and excited state species are enhanced, and the current pulses are weaker when the dielectric is thicker.

Although extensive research has been conducted on DBD characteristics, most studies have focused on atmospheric pressure conditions or planar geometries. A significant knowl-

edge gap remains regarding the discharge physics in rod-to-rod electrode configurations driven by nanosecond pulses at low pressure (e.g., 100 mbar). Specifically, the mechanism by which dielectric thickness modulates the local electric field reconfiguration and determines the transition between stable single-filament formation and stochastic multi-channel behavior has not been systematically elucidated. To address this, this work integrates 2D fluid modeling with time-resolved ICCD imaging to investigate the effect of dielectric thickness on the filamentary mode. We aim to clarify how the thickness-dependent electric field distribution influences the ionization intensity, channel morphology, and the stability of the discharge mode. This paper aims to investigate the effect of dielectric thickness on filamentary DBDs at low pressure, which is driven by a nanosecond pulse with a much shorter pulse width of 14 ns and a faster rise rate of 1.4 kV/ns. The rod-to-rod electrodes, which are similar to those of H Höft et al. [30], are used in this paper because stable mono-filament discharge can occur stably with this electrode; the experimental setup and simulation model are described in Section 2. In Section 3.1, the effect of the dielectric thickness of the cathode and anode on discharge is studied experimentally. After that, the development of discharge is simulated and the phenomenon of different dielectric thicknesses in the experiment is explained in Section 3.2. Finally, the conclusions are given in Section 4.

2. Experimental Setup and Simulation Model

An experimental platform was designed to investigate dielectric barrier discharge at 100 mbar in the vessel filled with N_2-O_2 mixtures (20% O_2 and 80% N_2), as shown in Figure 1. Before an experiment, the chamber is pumped to $p \leq 10^{-5}$ mbar. The gas flow into the vessel is controlled by mass flow controllers, and the total gas flow is adjusted to 10 slm $\pm$ 0.01 slm. Furthermore, as the chamber is pumped to an extremely low pressure before each experiment and the input gas is monitored by a flow meter, maintaining good airtightness for an extended period after gas input, it can be reasonably assumed that humidity does not influence the results in this experiment.

Rod-to-rod electrode structure is adopted in the experiment. The diameters of both the anode and the cathode are 10 mm. The inside of the electrode is iron metal, the surface is half-sphere quartz glass (the relative dielectric constant ε_r is 4), the thickness of the dielectric varies from 0 to 2 mm, and the electrode surfaces are polished smooth before the experiment. The gap between the electrodes is 3 mm. The positive unipolar nanosecond pulse voltage (V_a) generated by a high voltage power supply (FID GmbH, Model 50-50NX2, Burbach, Germany) is connected to the anode to drive DBDs. The voltage pulse width is 14 ns (full width at half maximum) with a pulse amplitude of 15.8 kV, the voltage rise time is 9 ns (defined by $T_r^{10–90\%}$, refers to the time required for the voltage to rise from 10% V_{max} to 90% V_{max}.) and the drop time is 11 ns (0–100%), as shown in Figure 2a. The selection of these specific pulse parameters plays a crucial role in the discharge dynamics. The high voltage rise rate of 1.4 kV/ns facilitates the establishment of a high overvoltage across the gap prior to breakdown, thereby generating a strong, reduced electric field that enhances ionization efficiency and streamer propagation velocity compared to slower pulse or AC excitations [30]. Furthermore, the ultrashort pulse width of 14 ns restricts the energy deposition window, ensuring that the discharge remains in a non-equilibrium filamentary mode and preventing the transition to a thermal arc, even under the high-intensity discharge conditions observed with the bare metallic anode. The applied voltage (V_a) is measured by a high voltage probe (PEMCH North Star, High Voltage PVM-5, Shenzhen, China), and the discharge current is measured by a Pearson current probe (Model 6585, Pearson Electronics, Palo Alto, CA, USA, 1 V/A, bandwidth is 400 Hz–250 MHz). Two current signals are recorded, the total electrical discharge current

(I_{tot}) and the displacement current (I_{dis}), and the conducting current $I_{con} = I_{tot} - I_{dis}$, as shown in Figure 2b. Both the voltage and current waveforms are recorded by an oscilloscope (Model MDO34 1 GHz, Tektronix, Shanghai, China). An intensified charge-coupled device (Model iStar DH334T, ICCD, Andor Technology Ltd., Northern Ireland, UK) is used to capture the discharge images through a quartz glass window, so the development of discharge and the discharge difference in different conditions can be observed.

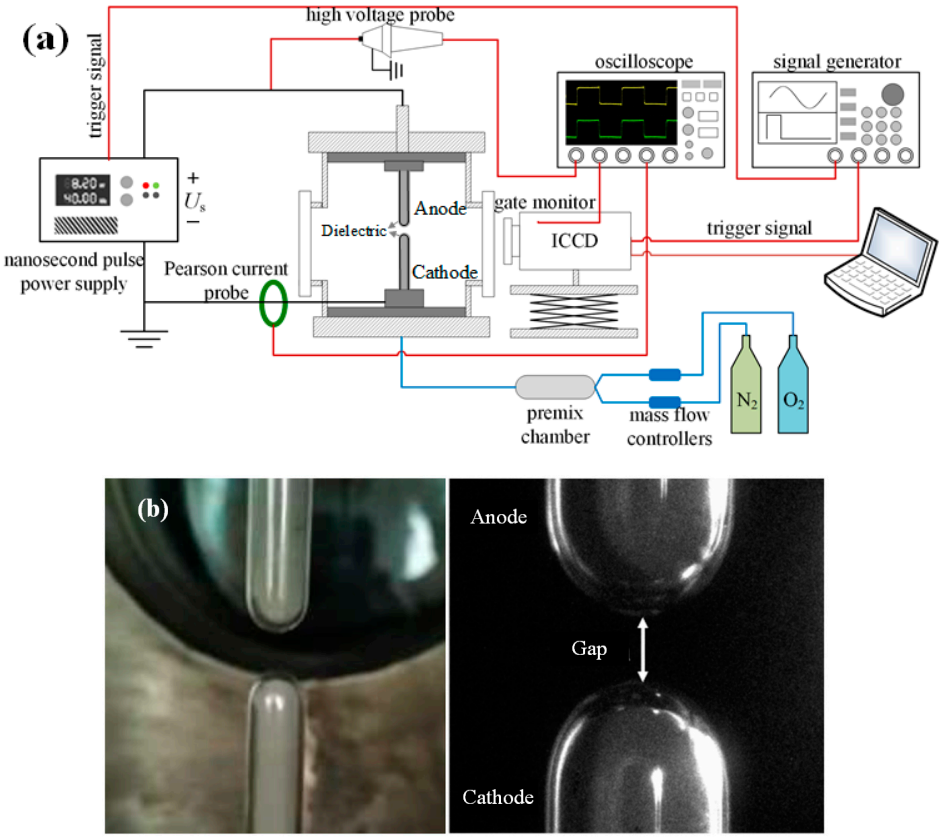

Figure 1. The experimental setup. (**a**) The setup diagram. The blue line represents the gas path. The red line represents measurement and control signals. The black line represents the circuit. (**b**) Images of the electrodes.

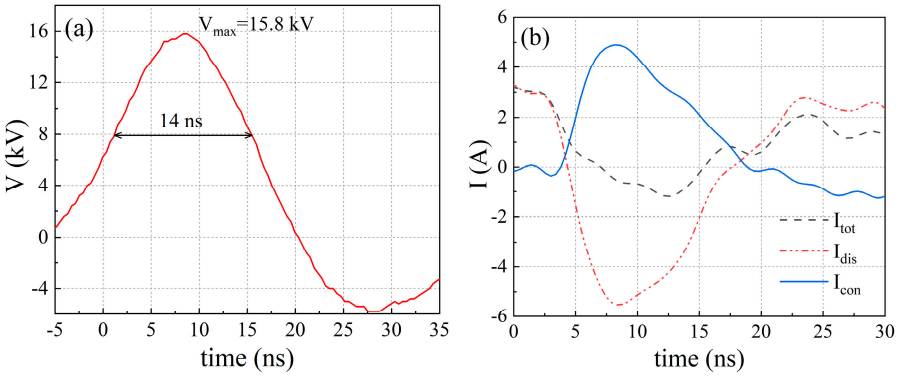

Figure 2. The waveforms of (**a**) nanosecond pulse voltage and (**b**) total electrical discharge current, displacement current and conducting current.

To ensure the reliability and reproducibility of the experimental results, critical operating parameters were strictly controlled within narrow uncertainty margins. The amplitude of the nanosecond pulse voltage was recorded during each discharge event, with deviations maintained within ±0.025 kV. The gas pressure was monitored in real-time using a vacuum

gauge with a resolution of 0.01 Pa, while the gas mixture ratio was precisely regulated by mass flow controllers with an accuracy of ±0.01 slm. Furthermore, the geometric precision of the dielectric tubes was machined to a tolerance of ±0.1 mm. These rigorous controls minimize the influence of experimental fluctuations, ensuring that the variations observed in the discharge characteristics are primarily attributed to the intrinsic physical mechanisms of the filamentary mode nanosecond-pulse DBD.

A 2D axisymmetric fluid model is used to simulate filamentary dielectric barrier discharge in rod-to-rod electrode structure at 100 mbar. A plasma solver PASSKEy (PArallel Streamer Solver with KinEtics, self coded) code coupling plasma and hydrodynamics [35,36] which was developed based on Fortran90 was used in this work to simulate the discharge in rod-to-rod electrodes. The simulations are performed on Sugon A620-G30 with two server processors (AMD EPYC™ 7281, Advanced Micro Devices Products Co., Ltd., Beijing, China, 32 core and 64 threads). It takes about 48 h to complete the 5.5 ns simulation.

The geometric structure, applied voltage, and gas composition are consistent with the experiment. Anode and cathode have similar structures. The radius of the electrode r is 5 mm, the gas gap d_g is 3 mm, and the surface dielectric thickness of the anode (D_a) and cathode (D_c) can be varied from 0 to 2 mm, which shows as 1 mm in Figure 3.

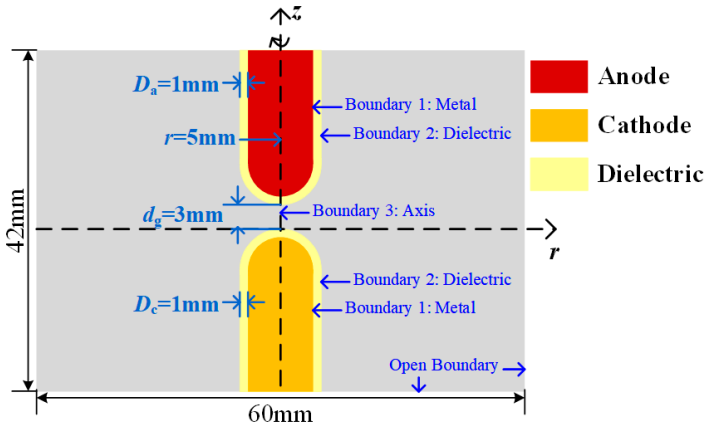

Figure 3. Simulation geometry and boundary conditions.

Detailed numerical methods and validations of PASSKEy can be found in previous publications [35,36], and only a brief description is given in this paper. The continuity equations combined with the drift-diffusion equations are solved to obtain a spatial and temporal distribution of species in Equations (1) and (2). An explicit UNO3 scheme (3rd order in time and space) coupled with the Strang operator for spatial splitting is used [37] to solve the drift term, an explicit 2nd order central discretization scheme is used to solve the diffusion term, and the stabilized Rouge–Kutta–Chebyshev scheme is used to solve plasma chemistry source [38].

$$\frac{\partial n_i}{\partial t} - \nabla \cdot \mathbf{\Gamma}_i = S_i + S_{\mathrm{ph}}, i = 1, 2, \ldots, N_{\mathrm{total}} \quad (1)$$

$$\mathbf{\Gamma}_i = D_i \nabla n_i + (q_i / |q_i|) \mu_i n_i \nabla \Phi, i = 1, 2, \ldots, N_{\mathrm{charge}} \quad (2)$$

where $\mathbf{\Gamma}_i$ is the flux of species, S_i is the source term of detailed chemical reactions, and S_{ph} is the photoionization source term for electrons and oxygen ions. Φ is the electrical potential, n_i is the number density of species, and q_i is the charge of species. D_i and μ_i are the diffusion coefficient and the mobility of charged species i.

The photoionization source term S_{ph} is solved by generalized Helmholtz equations, as shown in Equation (3).

$$S_{ph} = \sum_j S_{ph}^j \tag{3a}$$

$$\nabla^2 S_{ph}^j - (\lambda_i p_{O_2})^2 S_{ph}^j = -A_j p_{O_2}^2 I(R) \tag{3b}$$

$$\frac{g(R)}{p_{O_2}} = (p_{O_2} R) \sum_j A_j e^{-\lambda_i p_{O_2} R} \tag{3c}$$

where p_{O_2} is the partial pressure of O_2, $I(R)$ is the ionization source rate, $g(R)/p_{O_2}$ is the photoionization functions, λ_j and A_j are the three exponential fitting coefficients for photo-ionization functions taken from the work of Bourdon et al. [39]. R is the distance to the photoionization source, and i and j represent the photoionization of gas component i by gas component j.

Poisson's equations are solved to obtain the distribution of potential and electric field in Equation (4). At the dielectric–gas interface, the charge flux flowing towards the dielectric is stored at the edge of the grid cell, and an additional charge density is taken into account when solving Poisson's equation.

$$\nabla(\varepsilon(-\nabla\Phi)) = \sum_{i=1}^{N_{ch}} q_i n_i \tag{4}$$

Poisson's equation and Helmholtz equations are solved by a preconditioned conjugate-gradient solver, and A semi-implicit time integration scheme was used for Poisson's equation [40–43].

The local mean energy approximation (LMEA) is used in this paper. It has been proved that LMEA is more accurate when the grid is small at low pressure [44]. Furthermore, the local field approximation (LFA) simulation cannot obtain the sheath between the cathode surface discharge and the dielectric, because the strong field in the sheath will lead to the formation of "false ionization". Electronic properties, such as D_e, μ_e and rate constant of electron collision reactions are functions of the reduced electron mean energy in this paper.

The boundary conditions are summarized in Table 1. Note that the secondary electron emission coefficient of the dielectric almost has no effect on simulation results because the dielectric will soon be charged and the positive ions will hardly collide with the dielectric thereafter. Furthermore, the mobility of positive ions is very slow so positive ions around the streamer head cannot affect the rapidly propagating streamer. The kinetics scheme in this model is shown in Table 2, which contains 16 species, and 39 reactions.

Table 1. Boundary conditions in the simulation.

	Metal	**Dielectric**	**Open Boundary**
Potential	Anode: φ = U(t), cathode: $\varphi = 0$	$\partial\varphi/\partial t = 0$	/
Flow towards boundary	$\partial\mathbf{\Gamma_e}/\partial n = 0$, $\partial\mathbf{\Gamma_i}/\partial n = 0$	Charge accumulation	$\partial\mathbf{\Gamma_e}/\partial n = 0$, $\partial\mathbf{\Gamma_i}/\partial n = 0$
Flow away from the boundary	$\mathbf{\Gamma_e} = -\gamma\mathbf{\Gamma_i}$ *, $\mathbf{\Gamma_i} = 0$	$\mathbf{\Gamma_e} = -\gamma\mathbf{\Gamma_i}$ *, $\mathbf{\Gamma_i} = 0$	$\partial\mathbf{\Gamma_e}/\partial n = 0$, $\partial\mathbf{\Gamma_i}/\partial n = 0$

* The secondary electron emission coefficient γ is set to 0.01 for both metal and dielectric.

Initial plasma density with a Gaussian distribution is set on the anode surface, as shown in Equation (5), to enable the filamentary discharge to be ignited smoothly. In this equation, R and Z represent the radial and axial coordinates of the system.

$$n_{e0} = n_p = 10^{14} \times \exp\left(-\left(\frac{R}{3\times10^{-5}}\right)^2 - \left(\frac{Z\text{-}3\times10^{-3}}{7.5\times10^{-5}}\right)^2\right) + 10^9 (\mathrm{m}^{-3}) \tag{5}$$

Table 2. Kinetics scheme in the simulation.

No.	Reaction	Rate Constant *	Ref.
R1	$e + N_2 \rightarrow N_2^+ + e + e$	$f(\sigma,\varepsilon)$	[45]
R2	$e + O_2 \rightarrow O_2^+ + e + e$	$f(\sigma,\varepsilon)$	[46]
R3	$e + N_2 \rightarrow e + N_2(A^3\Sigma_u)$	$f(\sigma,\varepsilon)$	[45]
R4	$e + N_2 \rightarrow e + N_2(B^3\Pi_g)$	$f(\sigma,\varepsilon)$	[45]
R5	$e + N_2 \rightarrow e + N_2(C^3\Pi_u)$	$f(\sigma,\varepsilon)$	[45]
R6	$e + O_2 \rightarrow e + O + O$	$f(\sigma,\varepsilon)$	[46,47]
R7	$e + O_2 \rightarrow e + O + O(^1D)$	$f(\sigma,\varepsilon)$	[46,47]
R8	$N_2^+ + N_2 + M \rightarrow N_4^+ + M$	5×10^{-29}	[47,48]
R9	$N_4^+ + O_2 \rightarrow O_2^+ + N_2 + N_2$	2.5×10^{-10}	[47,48]
R10	$N_2^+ + O_2 \rightarrow O_2^+ + N_2$	6×10^{-11}	[47,48]
R11	$O_2^+ + N_2 + N_2 \rightarrow O_2^+ N_2 + N_2$	9×10^{-31}	[48]
R12	$O_2^+ N_2 + N_2 \rightarrow O_2^+ + N_2 + N_2$	4.3×10^{-10}	[48]
R13	$O_2^+ N_2 + O_2 \rightarrow O_4^+ + N_2$	1×10^{-9}	[48]
R14	$O_2^+ + O_2 + M \rightarrow O_4^+ + M$	2.4×10^{-30}	[47,48]
R15	$e + O_2 + O_2 \rightarrow O_2^- + O_2$	$2 \times 10^{-29} \times (300/T_e)$	[48]
R16	$e + O_2 \rightarrow O^- + O$	$f(\sigma,\varepsilon)$	[46]
R17	$O^- + O \rightarrow O_2 + e$	5×10^{-10}	[49]
R18	$O_2^- + O \rightarrow O_2 + O + e$	1.5×10^{-10}	[50]
R19	$e + N_4^+ \rightarrow N_2 + N_2(C^3\Pi_u)$	$2 \times 10^{-6} \times (300/T_e)^{0.5}$	[47]
R20	$e + N_2^+ \rightarrow N + N + 2.25$ eV	$2.8 \times 10^{-7} \times (300/T_e)^{0.5}$	[49]
R21	$e + O_4^+ \rightarrow O + O + O_2$	$1.4 \times 10^{-6} \times (300/T_e)^{0.5}$	[47,48]
R22	$e + O_2^+ \rightarrow O + O + 5.0$ eV	$2 \times 10^{-7} \times (300/T_e)$	[47,48]
R23	$O_2^- + O_4^+ \rightarrow O_2 + O_2 + O_2$	1×10^{-7}	[48]
R24	$O_2^- + O_4^+ + M \rightarrow O_2 + O_2 + O_2 + M$	$2 \times 10^{-25} \times (300/T_{gas})^{3.2}$	[48]
R25	$O_2^- + O_2^+ + M \rightarrow O_2 + O_2 + M$	$2 \times 10^{-25} \times (300/T_{gas})^{3.2}$	[48]
R26	$O^- + N_2^+ \rightarrow O + N + N$	1×10^{-7}	[49]
R27	$N_2(C^3\Pi_u) + N_2 \rightarrow N_2(B^3\Pi_g,v) + N_2$	1×10^{-11}	[47]
R28	$N_2(C^3\Pi_u) + O_2 \rightarrow N_2 + O + O(^1D)$	3×10^{-10}	[47]
R29	$N_2(C^3\Pi_u) \rightarrow N_2 + h\nu$	2.38×10^7	[48]
R30	$N_2(B^3\Pi_g) + O_2 \rightarrow N_2 + O + O$	3×10^{-10}	[47]
R31	$N_2(B^3\Pi_g) + N_2 \rightarrow N_2(A^3\Sigma_u) + N_2(v)$	1×10^{-11}	[47]
R32	$N_2(A^3\Sigma_u) + O_2 \rightarrow N_2 + O + O$	$2.5 \times 10^{-12} \times (T_{gas}/300)^{0.5}$	[47]
R33	$O(^1D) + O_2 \rightarrow O + O_2$	$3.3 \times 10^{-11} \times \exp(67/T_{gas})$	[47]
R34	$O(^1D) + N_2 \rightarrow O + N_2$	$1.8 \times 10^{-11} \times \exp(107/T_{gas})$	[47]
R35	$O + O_2 + O_2 \rightarrow O_3 + O_2$	$6.9 \times 10^{-34} \times (300/T_{gas})^{1.25}$	[49]
R36	$O + O_2 + N_2 \rightarrow O_3 + N_2$	$6.9 \times 10^{-34} \times (300/T_{gas})^2$	[49]
R37	$O + O_3 \rightarrow O_2 + O_2$	$2 \times 10^{-11} \times \exp(-2300/T_{gas})$	[49]
R38	$N_2^+ + O_3 \rightarrow O_2^+ + O + N_2$	1×10^{-10}	[49]
R39	$e + O_3 \rightarrow O_2^- + O$	1×10^{-9}	[49]

* Rate constants are given in s^{-1}, cm^3s^{-1}, and cm^6s^{-1}. Electron temperature T_e is given in K. Gas temperature T_{gas} is given in K.

3. Results and Discussion

3.1. Experimental Results of DBD with Different Dielectric Thicknesses

To study the effect of dielectric thickness on discharge characteristics, six groups of experiments are set up as shown in Table 3. Their rod electrode diameters are the same (10 mm) and only the dielectric thicknesses are different. D_a-D_c is used to represent each group in this paper. For example, the first group is represented as 1 mm-1 mm.

Table 3. Electrode geometric parameters.

No.	Anode Dielectric Thickness (D_a)	Cathode Dielectric Thickness (D_c)	Anode Diameter	Cathode Diameter
1	1 mm	1 mm	10 mm	10 mm
2	1 mm	2 mm	10 mm	10 mm
3	2 mm	1 mm	10 mm	10 mm
4	2 mm	2 mm	10 mm	10 mm
5	0 (metal)	1 mm	10 mm	10 mm
6	0 (metal)	2 mm	10 mm	10 mm

Figure 4a presents the applied voltage and the conduction current ($I_{con} = I_{tot} - I_{dis}$) of 1 mm-1 mm. The current starts to rise around 3 ns when the voltage across the gap reaches the breakdown threshold, peaks at 4.9 A at 8.2 ns. Then the current decreases, not only because the applied voltage falls but also because charges accumulate on the dielectric surface forming a space charge field and decreasing the electric field between electrodes. Only one discharge occurs due to the applied pulse voltage having a very short pulse width. However, two discharges will occur, one at the rising slope and one at the falling slope, if the applied pulse voltage has a longer pulse width (several microseconds) [30,51,52]. ICCD images of the discharge are shown in Figure 5. Although each image is not from the same discharge, Figure 5 can still illustrate the development of DBD since the discharge is stable and repeatable. There are two light spots on the electrode surface, the discharge images of 6 ns and 7 ns, for example, the spots are marked by dotted lines, they are not generated by the discharge directly, but generated by reflecting the discharge light in the channel because the dielectrics are glass. The discharge breaks down the gas gap within the 2 ns gate width, becomes stronger and stronger until 8 ns and then is gradually extinguished. The discharge images are consistent with the current, which is also largest at around 8 ns and then gradually decreases. Furthermore, the surface discharges spread on both the anode and cathode dielectric.

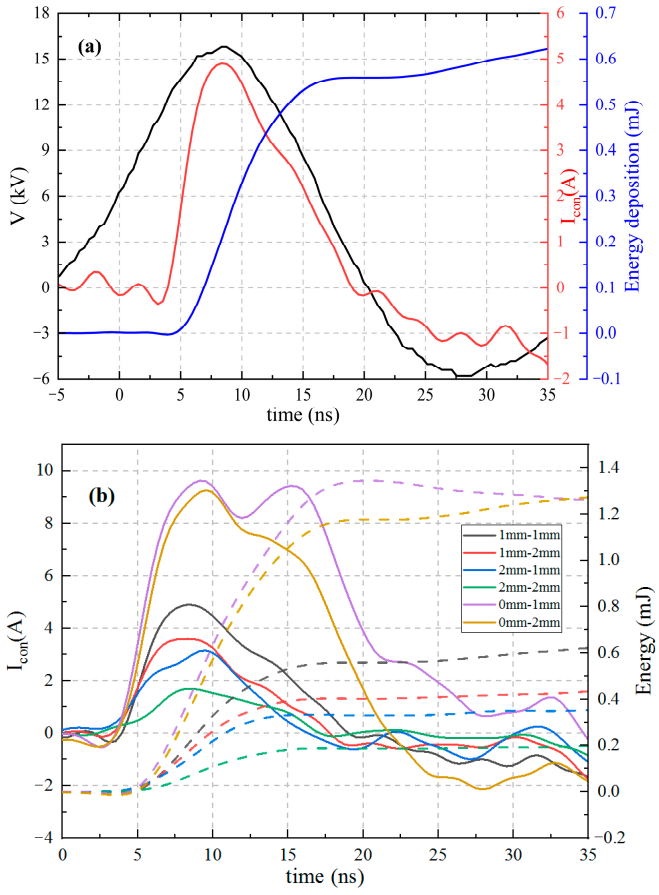

Figure 4. Voltage and current waveforms captured in the experiment. (**a**) The applied voltage, conduction current and energy deposition of 1 mm-1 mm case. (**b**) The conduction current and energy deposition with different D_a and D_c. Solid lines denote current, while dashed lines denote deposited energy.

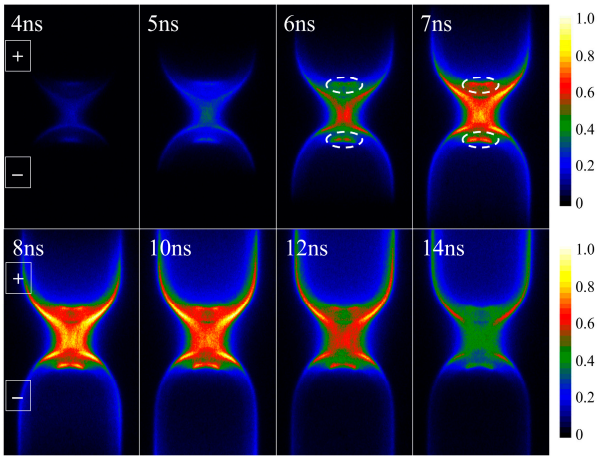

Figure 5. ICCD images of discharge of DBD in 100 mbar air when D_a and D_c are 1 mm (ICCD gate width is 2 ns, gain is 2500, five subsequent DBDs are accumulated, with an interval of 5 s between each DBD). The intensity is normalized for each image. The light spots inside the dotted line are not generated by the discharge directly, but reflected by the glass dielectric.

Figure 4b presents the conduction current with different dielectric thicknesses of the anode and cathode. When both electrodes are covered by the dielectric, the larger the total thickness of the dielectric ($D_a + D_c$), the weaker the current. It is worth noting that when $D_a \neq D_c$ but $D_a + D_c$ is the same (groups 2 and 3), the increase in D_a or D_c will lead to a decrease in current, and there is little difference in current amplitude. ICCD images of the first four groups are shown in Figure 6. The discharge is weaker with the thicker dielectric, which corresponds to the weaker current.

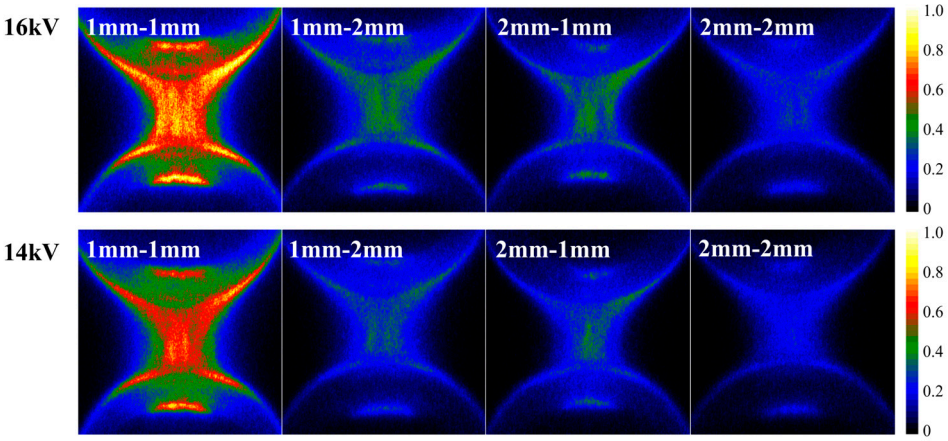

Figure 6. ICCD images of the first four groups with different D_a and D_c at 7 ns. (ICCD gate width is 2 ns, gain is 2500, the image of a single DBD is taken). The intensity is normalized for each image.

Regarding the energy per pulse calculations, the energy deposition is calculated by performing a time integration of the product of the applied voltage and the conduction current, also shown in the figure. As illustrated in Figure 4a (taking the 1 mm-1 mm case as a typical example), the energy deposition process is highly transient and synchronized with the discharge current pulse. The energy rises steeply during the high-current phase (approximately 5–15 ns) where the voltage is near its peak (0.56 mJ), and then stabilizes as the conduction current decays to zero, indicating that the effective energy injection is confined to the nanosecond-scale discharge duration. Furthermore, Figure 4b compares the temporal evolution of energy deposition across all dielectric configurations. The results demonstrate a clear inverse correlation between total dielectric thickness and deposited

energy. The bare metallic anode cases exhibit the highest energy deposition (reaching approximately 1.3–1.4 mJ), which corresponds to the most intense plasma generation. In contrast, increasing the dielectric thickness on either electrode significantly limits the discharge current and consequently suppresses the energy deposition, with the 2 mm-2 mm case showing the lowest energy value (approximately 0.2 mJ).

The discharge channel is defined as the area with an intensity larger than 0.2 using the normalized standard in Figures 5 and 6, and the channel diameters in the middle of the gas gap with different D_a and D_c are compared in Figure 7. The channel diameter is the average of twenty images. With the increase in $D_a + D_c$, the channel diameter decreases, and the change in diameter does not change a lot when $D_a + D_c$ is the same but $D_a \neq D_c$. In addition, the diameter is bigger when the applied voltage is larger.

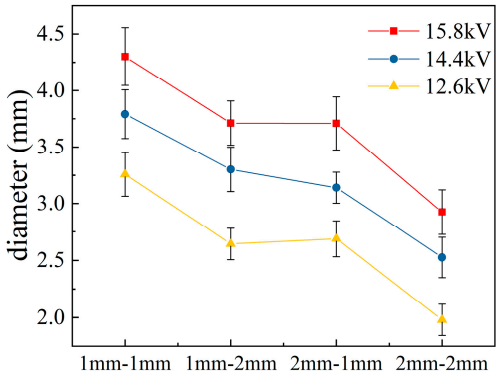

Figure 7. Comparison of discharge channel diameters with different D_a and D_c.

The discharge characteristics when both electrodes are covered by dielectric have been analyzed above; when the anode is metal without dielectric covering is further analyzed below. The current pulse width increases significantly when the anode is metal as shown in Figure 4. The maximum current is 9.6 A, while it is 4.9 A when both electrodes are covered with 1 mm dielectrics. The ICCD images are shown in Figure 8. The intensity increased significantly, which is about 2.5 times stronger than that of the 1 mm-1 mm group. There are two modes of discharge: mode A is a single discharge with a stable discharge position and uniform distribution of intensity, and mode B has at least two discharges with random locations and non-uniform distribution of intensity. In the group of 0–2 mm, most of the discharge is mode A, and mode B appears sometimes. However, in the 0–1 mm group, most of the discharge is mode B, which is why the current has double peaks, as shown in Figure 4.

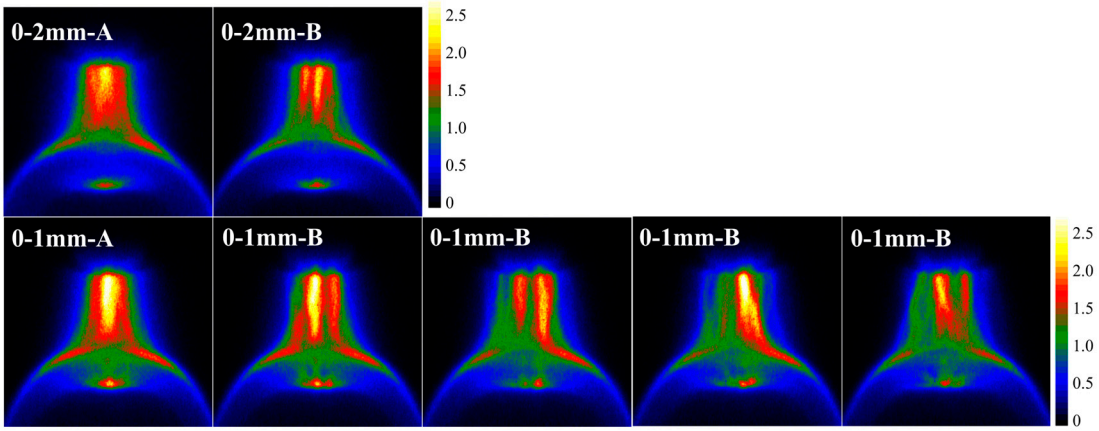

Figure 8. ICCD images of the last two groups with different D_a and D_c at 7 ns. (ICCD gate width is 2 ns, gain is 2500, the image of a single DBD is taken). The intensity is normalized for each image.

3.2. Simulation Results of DBD with Different Dielectric Thicknesses

3.2.1. Discharge Propagation

The propagation of DBD under a nanosecond pulse is very fast, the discharge breaks down the gap within 2 ns as observed in the experiment shown in Figure 5, but detailed observation and analysis of the propagation cannot be easily carried out through experiments. Therefore, a two-dimensional axisymmetric model is established to better understand the discharge propagation process. The simulation uses the same parameters as the experiment (a nanosecond pulse voltage of 15.8 kV is applied to the anode, 20% O_2 and 80% N_2 in 100 mbar, and the gas gap is 3 mm). The discharge propagation can be divided into two stages: (I) the volume discharge stage and (II) the surface discharge stage.

Figure 9 presents the evolution of electron density during the volume discharge stage. The discharge ignites at 2.2 ns and breaks down in 0.5 ns. Promoted by avalanche and photoionization, the volume discharge develops towards the cathode in the shape of a water droplet and a protrusion of the discharge head is observed at 2.4 ns. The protrusion gradually submerges in the channel as the discharge develops. Thereafter, the discharge develops towards the cathode and finally breaks down the gap. To investigate the formation of the protrusion, the space–time evolution of electrons from 1.6 ns to 2.4 ns is shown in Figure 10. To show the electron evolution more clearly, the scale of electron density is different. Plasma clouds are generated near the cathode and anode at 1.6 ns when the discharge does not ignite. Electrons near the anode multiply and gradually form the discharge, while the electrons near the cathode move towards the anode with the promotion of the applied electric field, the electron density in the cloud increases and finally merges with the volume discharge at 2.4 ns.

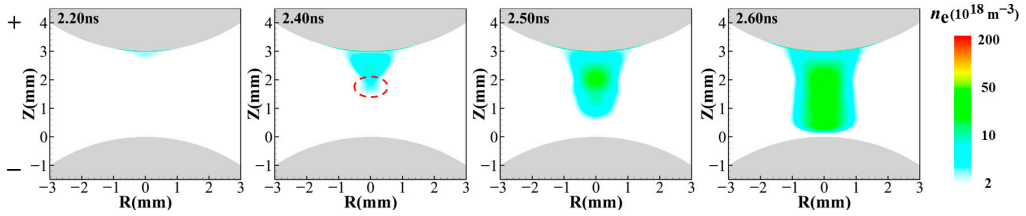

Figure 9. The evolution of electron density during the volume-discharge stage.

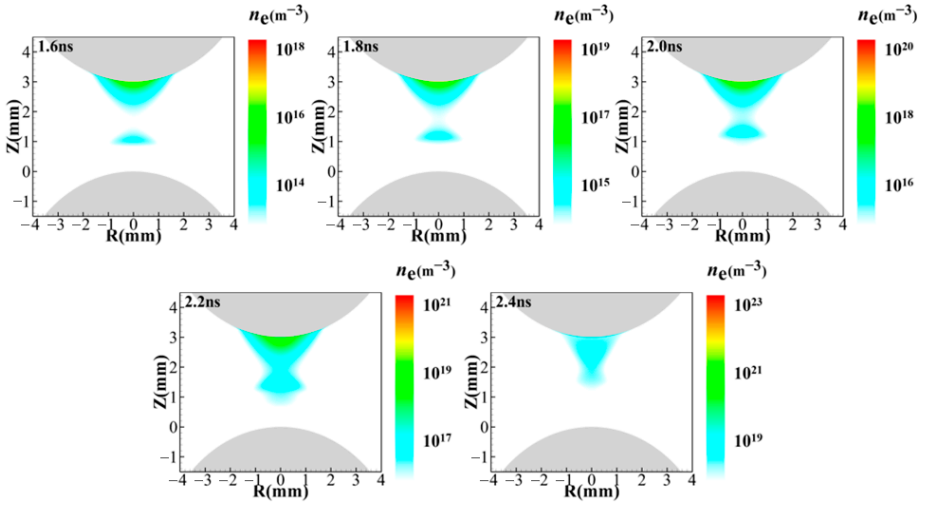

Figure 10. The evolution of electron cloud near cathode before 2.4 ns.

The head position and velocity of discharges are shown in Figure 11a. The development velocity of volume discharge increases first and then decreases, reaching the peak (about 12 mm/ns) at 2.4 ns when the protrusion is formed. The effect of plasma cloud on

velocity is due to charge separation. With the applied electric field, the head of the cloud is mainly electrons, and the tail is mainly positive ions. When the volume discharge meets the cloud, the electrons in the cloud head provide a large number of seed electrons for the development of volume discharge, so its velocity is rapidly increased from 4 mm/ns to 12 mm/ns.

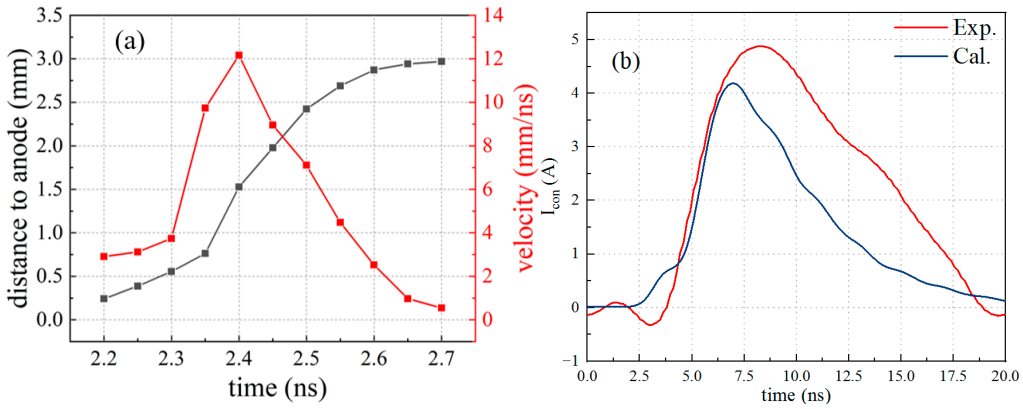

Figure 11. Discharge characteristics (**a**) Position (black line) and velocity (red line) of volume discharge. (**b**) Comparison between experiment and simulation on the discharge current.

The comparison between experiment and simulation on the discharge current is shown in Figure 11b. The experimental peak current is 4.9 A, while the simulated peak current is approximately 4.18 A. This deviation of about 15% is considered a reasonable agreement for a fluid model, given the complexity of reaction kinetics and photoionization approximations. This indicates that the order of magnitude of electron density derived from the model is reliable. Regarding the discharge initiation and breakdown process, the simulation predicts a faster discharge onset. The simulated current begins to rise significantly around 2.5 ns, whereas the experimental current rises sharply around 4.0 ns. This discrepancy may be attributed to the initial seed electron density settings in the simulation or the idealized voltage application in the model, which overlooks the inherent propagation delays in experimental transmission lines. However, it cannot be overlooked that there is still some error in the shape of the calculated discharge current compared to the experimental results.

Figure 12 presents the electron density and electric field during the surface discharge stage. The surface discharge on the cathode dielectric is a positive streamer and on the anode dielectric is a negative streamer. The scale of the electric field is different: 0–3000 Td for discharge on the cathode dielectric, and 0–1500 Td for discharge on the anode dielectric. The electron density in the channel is about 1×10^{19} m^{-3}, and it will be larger near the surface of the dielectric. The electric field in the channel is small (below 400 Td) but it is very large at the discharge head (above 1000 Td). Furthermore, a 0.06 mm sheath is formed between the positive surface streamer and the cathode, which has a strong electric field (above 3000 Td). The sheath is also observed in ref. [53], although their discharge is in argon at atmospheric pressure. However, there is no sheath on the anode surface because electrons and other negative ions move toward the dielectric surface in the negative streamer. It can also be observed that the electric field in the dielectric covered by surface discharge is gradually stronger with the development of discharge. This is because many charges accumulate on the surface which lead to the polarization of the dielectric and makes the dielectric electrogenic.

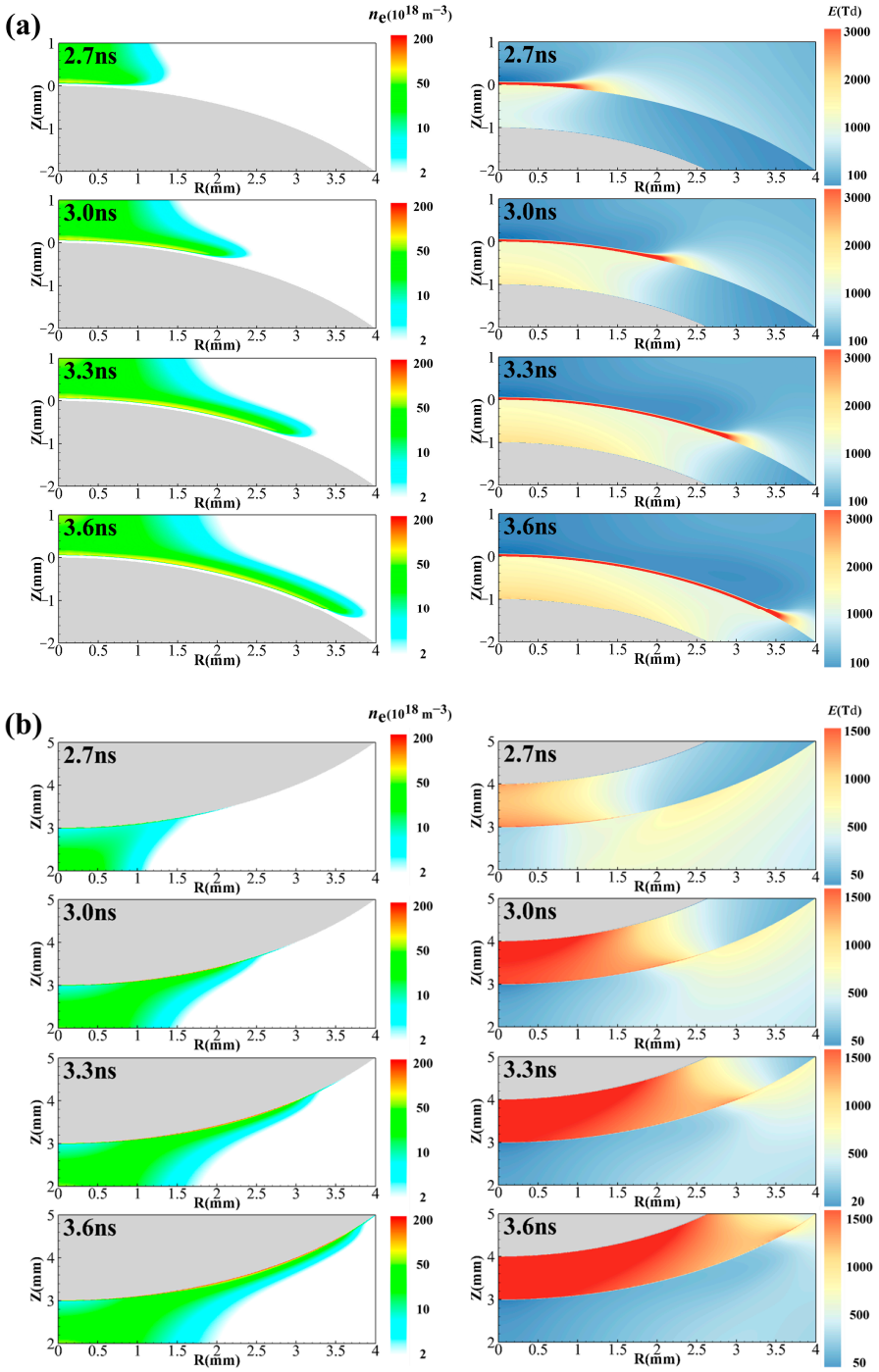

Figure 12. The evolution of electron density (**left**) and electric field (**right**) during the surface discharge stage. (**a**) On the cathode dielectric and (**b**) on the anode dielectric.

The length and velocity of surface discharge are shown in Figure 13. For discharge on the cathode surface, it develops from about R = 1 mm, the velocity gradually decreases from 4.25 mm/ns and finally stabilizes at 2.5 mm/ns. For discharge on the anode surface, it develops from about R = 1.8 mm, the velocity is almost stable at 2.5 mm/ns. The positive streamer on the cathode surface evolved from the volume discharge. The discharge channel widens and deflects along the dielectric surface with the promotion of the radial electric field when the volume discharge breaks down the gap. Therefore, the ionization of the positive streamer head is more intense and develops faster in the initial stage of surface discharge.

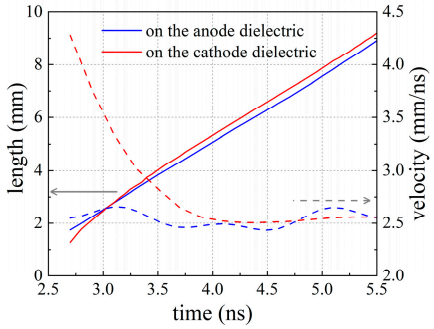

Figure 13. Length (solid line) and velocity (dash line) of surface discharge on the cathode and anode dielectric.

The change in discharge channel diameter is shown in Figure 14a, the definition of discharge channel in the simulation is the area with electron density greater than 1×10^{19} m^{-3}, and it is the area with intensity larger than 0.2, 0.1, and 0.5 in the experiment. Figure 14 shows the diameter of the gap middle. The diameter increases first and then becomes stable both in the experiment and the simulation, and the diameter eventually stabilizes around 5 mm. To explain the change in diameter, the electric field at the boundary of the discharge channel (where the electron density is 1×10^{19} m^{-3}) at the middle gap at different times is extracted, as shown in Figure 14b. The electric field at the boundary is about 600 Td at the breakdown which means the ionization is intense, the electrons multiply rapidly and move radially, causing the discharge channel to widen. The electric field is lower than 100 Td after 7.5 ns, where the effective Townsend ionization coefficient is very small or even lower than the effective attachment coefficient. The ionization is greatly reduced and electron attachment becomes increasingly important, resulting in the diameter of the discharge channel no longer increasing.

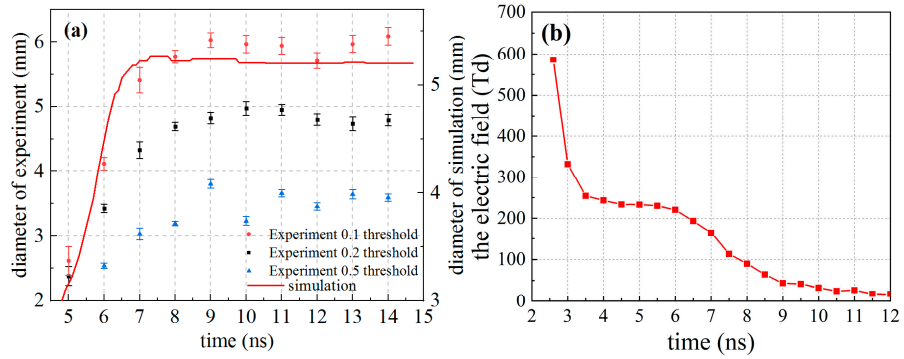

Figure 14. (**a**) Comparison of discharge channel diameter between experiment (under different thresholds) and simulation. (**b**) The electric field at the channel boundary during the discharge development.

The comparison of discharge images between the experiment and simulation is shown in Figure 15. Since random discharges cannot be simulated in our fluid model, only stable discharges (mode A) are compared here. As for the random discharges observed in the experiment, one of the main reasons for positive streamer branching is considered to be the stochastic discharge process. As shown in the results of Wang et al. [54], they used Monte Carlo photoionization instead of Helmholtz photoionization to simulate the streamer discharge-branching process and gained good agreement with the experimental results. Therefore, because our fluid model does not incorporate any parameters that could introduce random or stochastic perturbations, we are unable to reproduce the branching phenomenon in our simulations that arises from stochastic factors (such as stochastic

photoionization or random local heating). The discharge is in the shape of a vertical "H" when D_a is not 0, and in the shape of an inverted "T" when D_a is 0. It can be observed that the electron density is lower and the discharge intensity is weaker near the dielectric both in the simulation and the experiment. The main sources of electrons on the dielectric surface are electron collision ionization and photoionization. Electrons, positive and negative ions accumulate on the surface and develop into surface discharge. The main sources of electrons on the metal surface are electron collision ionization, photoionization, and secondary electron emission, and ions do not accumulate on the metal surface, so the electron density is larger and there is no region with lower electron density on the metal surface. The electric field near the dielectric is below 100 Td and the attachment coefficient is bigger than the ionization coefficient. More intense electron attachment leads to a low electron density region. The electric field is stronger in the middle of the gap and near the metal anode where the ionization is more intense and the electron density is larger.

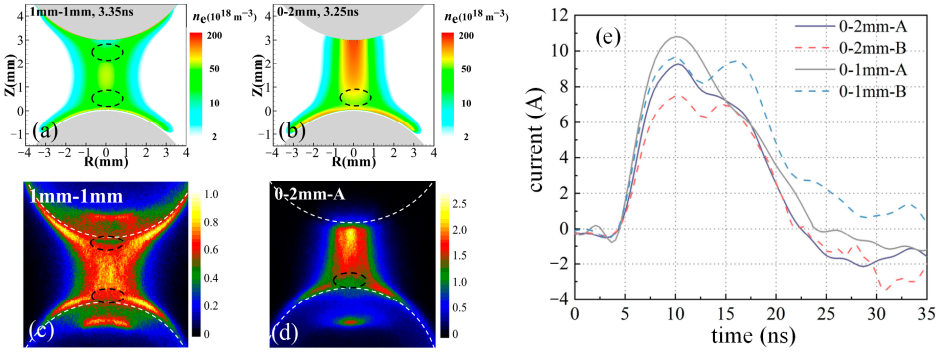

Figure 15. The electron density in the simulation (**a**) when D_a is not 0 and (**b**) D_a is 0. ICCD images in experiment (**c**) when D_a is not 0 and (**d**) D_a is 0. (**e**) The discharge current waveform when D_a = 0.

To further investigate the two discharge modes, we performed a statistical analysis of the discharge morphology based on 50 consecutive discharge images. In configurations where both electrodes are covered by dielectric layers, we observed that while the discharge intensity and channel diameter decrease with increasing total dielectric thickness, the discharge morphology remains unaffected, consistently presenting a stable single-filament structure. Conversely, for the bare metallic anode cases D_a = 0, the external voltage is applied directly to the gas gap, resulting in a significant enhancement in discharge intensity—approximately 2.5 times that of the 1 mm-1 mm case—which indicates a marked improvement in plasma generation efficiency. However, the morphology at D_a = 0 becomes bimodal, exhibiting either Mode A (stable single-filament with uniform intensity) or Mode B (stochastic multi-filament with random positions). Our statistical results show that for the 0 mm–2 mm configuration, Mode A dominates with a probability of 85%, with Mode B appearing only 15% of the time. In contrast, for the thinner 0 mm–1 mm configuration, the probability of Mode B rises significantly to 40%. This indicates that under the bare metallic anode condition, a thinner cathode dielectric leads to stronger stochasticity. This increased randomness and the frequent occurrence of multi-filaments in the 0 mm–1 mm case provide a direct physical explanation for the double-peak structure observed in the measured current waveforms shown in Figure 15e.

3.2.2. Comparison of DBDs with Different Dielectric Thicknesses

Figure 16 shows the electric field along the Z-axis at 0 ns and after the breakdown. At 0 ns, the applied voltage is about 6 kV and the discharge is not ignited. It can be seen that the smaller the $D_a + D_c$, the stronger the electric field is. When $D_a + D_c$ is the same but $D_a \neq D_c$, only the electric field near the anode and cathode has a little difference, and

it is stronger on the side with thinner dielectrics. The effect of the electric field at 0 ns is present as follows: first, the discharge conditions can be satisfied earlier when $D_a + D_c$ is small and the discharge can be ignited earlier; second, the ionization is more intense when the electric field is large, which will lay the foundation for the difference in current under different dielectric thicknesses. Figure 16b shows the electric field after discharge breakdown. Although the applied voltage is much higher than that at 0 ns, the electric field of the *Z*-axis is weaker because the discharge channel has formed and the electric field is shielded. When D_a is not 0 (that is, both electrodes are covered by a dielectric), it can be observed that the electric field is larger when the dielectric is thinner although the electric field difference is small. When D_a is 0 (that is, the anode is metal), the electric field is much larger due to the applied voltage acting directly on the gas gap rather than through the dielectric.

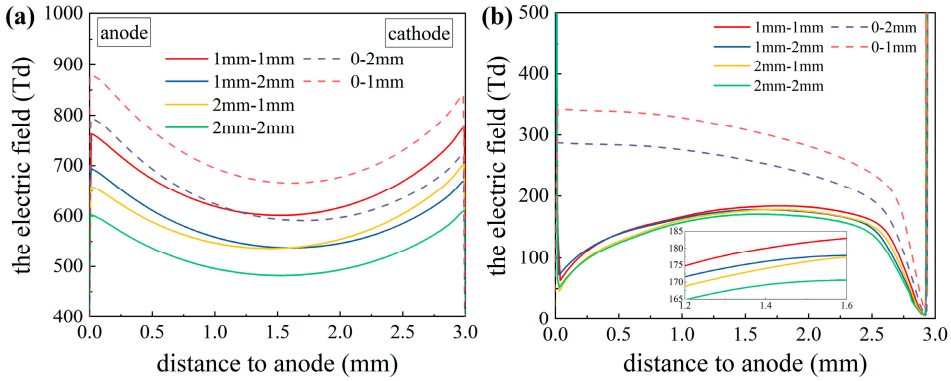

Figure 16. The electric field along the Z-axis (**a**) at 0 ns and (**b**) after the breakdown.

The distribution of electron density and electric field are compared in Figure 17. The electron density increases when the dielectric is thinner, and the maximum electron density is about 5×10^{19} m^{-3} in the volume discharge channel when D_a is not 0. However, it increases to above 2×10^{20} m^{-3} when D_a is 0. The difference in electron density is related to the electric field. The electron collision, ionization, and excitation are more intense with the larger electric field, which means the discharge is more intense and the current is larger. It can be seen in Figure 17b that the electric field is small in the discharge channel while it is larger in the dielectric, because a large amount of space charge (negative charge on the surface of the anode dielectric and positive charge on the surface of the cathode dielectric) is accumulated on the surface of the dielectric after the discharge breakdown, and the electric potential is concentrated on the surface and in the dielectric. Furthermore, the electric field in the dielectric is weaker when the dielectric is thicker. When the anode is metal, the electric field of the cathode dielectric is much stronger because most of the electric potential is concentrated on the cathode dielectric.

It has been observed in experiments that the diameter of the discharge channel increases with thinner dielectric thickness, and the difference in diameter is small when $D_a + D_c$ is the same (Figure 7). Figure 18a shows the difference in diameter with different D_a and D_c from discharge breakdown to 5.5 ns. The results of simulations and experiments are consistent (as shown in Figure 7), the diameter developed to about 6 mm at 5.5 ns when $D_a = D_c = 0.5$ mm, while the diameter is only 1.5 mm at 5.5 ns when $D_a = D_c = 2$ mm. The electric field at the boundary of the discharge channel is shown in Figure 18b. The horizontal axis t-t_b represents the time for surface discharge development where t_b is the time when the volume discharge breaks down the air gap. The electric field at the boundary of the discharge channel is very strong at the time of breakdown and becomes stable with the development of discharge. Furthermore, the electric field is stronger with the increase in electrode dielectric thickness

D_a + D_c during the development of surface discharge, which means a more intense ionization and a higher electron density, resulting in the increase in channel diameter.

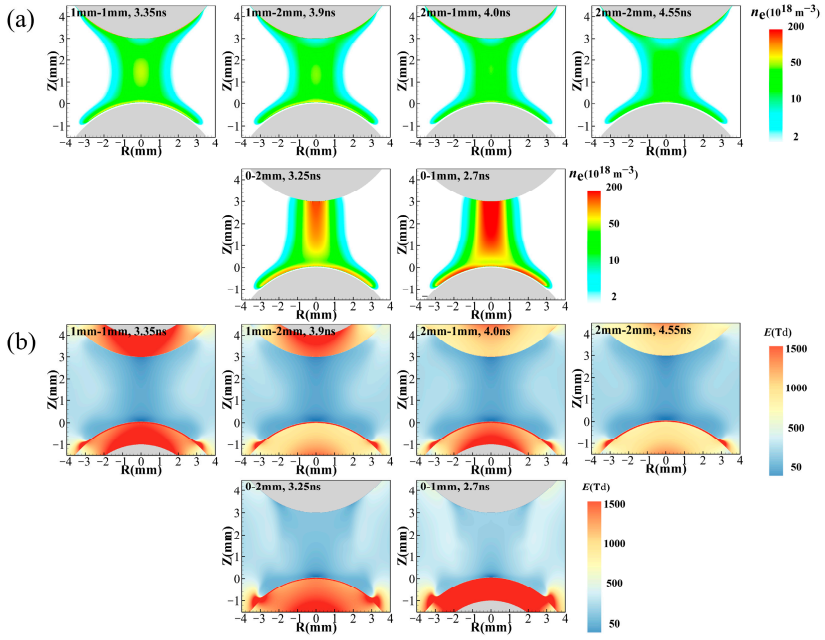

Figure 17. The distribution of (**a**) electron density and (**b**) electric field with different D_a and D_c.

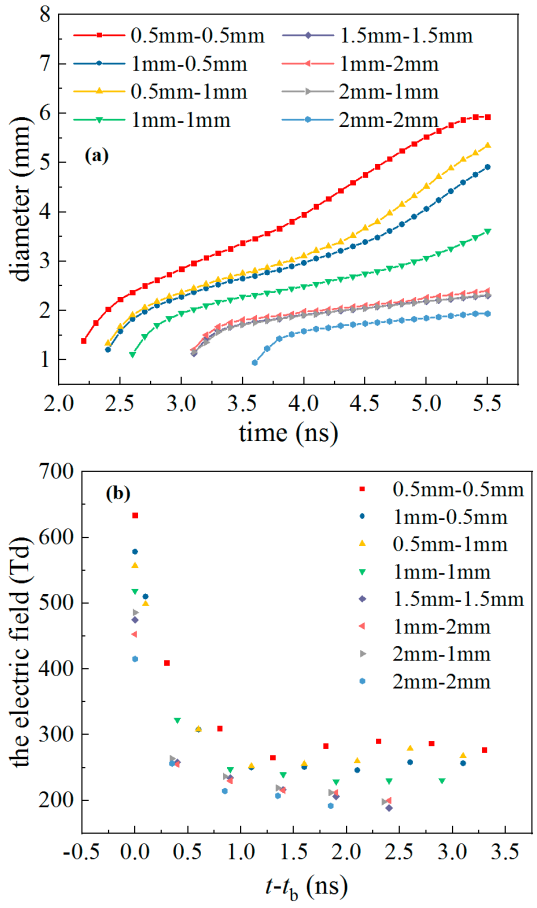

Figure 18. (**a**) The difference in diameter with different D_a and D_c from discharge breakdown to 5.5 ns. (**b**) The electric field at the boundary of the discharge channel. t_b is the time when the discharge breaks down the air gap.

4. Conclusions

In this work, the evolution of dielectric barrier discharge with rod-to-rod electrodes at 80 mbar in N_2-O_2 mixtures air (20% O_2 and 80% N_2) and the effects of surface dielectric thickness on the characteristics are investigated. The discharge is driven by a positive unipolar nanosecond pulse voltage with 15.8 kV amplitude, 9 ns rise time (defined by $T_r^{10–90\%}$), and 14 ns pulse width. Operating at this pressure allows us to generate stable mono-filaments or controlled multi-filaments, facilitating the detailed investigation of the streamer discharge mechanism and the specific effects of dielectric thickness on discharge characteristics. The combination of low pressure and nanosecond-pulse excitation is beneficial for producing high-energy electrons and active species. Our simulation results indicate that the reduced gas density at low pressure, combined with the strong electric field driven by the fast rise-time pulse, leads to more intense ionization. From a numerical modeling perspective, the fluid model using the local mean energy approximation (LMEA) is proved to be more accurate when the grid is small at low pressure. Experimentally, the lower pressure expands the spatial scale of the discharge channels, allowing for clearer observation of the surface discharges and discharge channel evolution using the intensified charge-coupled device.

The conclusions can be summarized as follows.

After the volume discharge ignites, it merges with the plasma cloud. Charge separation occurs in the cloud, and electrons in the head provide seed electrons for the volume discharge, causing the discharge velocity to increase rapidly. The positive surface streamer on the cathode dielectric is converted from volume discharge. Compared with the negative surface streamer on the anode, the ionization of the positive surface streamer head is more intense, so it is easier to ignite, and the discharge develops faster.

The decrease in the total dielectric thickness ($D_a + D_c$) leads to larger currents, stronger discharges, and wider discharge channels whether the thickness of the cathode (D_c) is the same as that of the anode (D_a) or not. The discharge characteristics are similar when $D_a + D_c$ is the same but $D_a \neq D_c \neq 0$. If the anode is a metal electrode ($D_a = 0$), the discharge will be much more intense and the current will increase significantly; in addition, the discharge presents two modes: a stable mono-filament discharge mode and a random multi-filament discharge mode.

The observed results are related to the change in the electric field in simulation. The currents are larger with smaller $D_a + D_c$ because the dielectric thickness changes the electric field configuration and the electric field is stronger with smaller $D_a + D_c$ (it is much stronger when $D_a = 0$). Driven by a stronger electric field, the ionization is more intense and the electron density is larger, eventually leading to an increase in current. The discharge channels are wider with smaller $D_a + D_c$ because the electric field at the channel boundary is stronger with the decrease in dielectric thickness which means more electrons are produced at the channel boundary, leading to a wider discharge channel. Finally, the scope of this study should be noted. The experiments and simulations were conducted under low-pressure conditions (100 mbar) using a rod-to-rod geometry to specifically isolate the filamentary structures and resolve the spatio-temporal dynamics of the discharge channels. While the absolute values of discharge parameters (e.g., breakdown voltage and current density) will vary at atmospheric pressure or with different gas mixtures due to changes in collision frequencies and photoionization rates, the core mechanism revealed in this work is generalizable. Specifically, the fundamental role of dielectric thickness in modulating the local electric field enhancement and determining the transition between stable (Mode A) and stochastic (Mode B) regimes is applicable to a broad range of nanosecond-pulse dielectric barrier discharge configurations.

https://doi.org/10.3390/plasma9010004

From an application perspective, these findings suggest that dielectric thickness serves as a critical tuning parameter for optimizing plasma reactors. For applications requiring high energy deposition rates, such as plasma-assisted combustion or waste gas treatment, a thinner dielectric layer is preferable to maximize discharge intensity. Conversely, for processes demanding high spatial uniformity and reproducibility, such as precise surface modification or thin film deposition, increasing the dielectric thickness provides a robust method to stabilize the discharge and suppress stochastic filamentary behavior.

Author Contributions: Conceptualization, A.S.; methodology, Y.G. and Y.Z.; software, Y.Z.; validation, A.S. and Y.G.; formal analysis, Y.G. and Y.Z.; investigation, Y.G.; data curation, Y.L.; writing—original draft preparation, A.S., Y.G. and Y.L.; writing—review and editing, A.S.; visualization, Y.L.; supervision, A.S. and Y.Z.; project administration, A.S.; funding acquisition, A.S. All authors have read and agreed to the published version of the manuscript.

Funding: Project supported by the Natural Science Basic Research Program of Shaanxi (No. 2024ZY-JCYJ-01-06).

Data Availability Statement: The data that support the findings of this study are available from the corresponding author upon reasonable request.

Conflicts of Interest: Author Yanru Li was employed by the company State Grid Gansu Electric Power Company Electric Power Research Institute. The remaining authors declare that the research was conducted in the absence of any commercial or financial relationships that could be construed as a potential conflict of interest.

References

1. Laroussi, M. Low Temperature Plasma-Based Sterilization: Overview and State-of-the-Art. *Plasma Process. Polym.* **2005**, *2*, 391–400. [CrossRef]
2. Machala, Z.; Graves, D.B. Frugal Biotech Applications of Low-Temperature Plasma. *Trends Biotechnol.* **2018**, *36*, 579–581. [CrossRef]
3. Ranjitha Gracy, T.K.; Gupta, V.; Mahendran, R. Influence of low-pressure nonthermal dielectric barrier discharge plasma on chlorpyrifos reduction in tomatoes. *J. Food Process Eng.* **2019**, *42*, e13242. [CrossRef]
4. Tanino, T.; Matsui, M.; Uehara, K.; Ohshima, T. Inactivation of Bacillus subtilis spores on the surface of small spheres using low-pressure dielectric barrier discharge. *Food Control* **2020**, *109*, 106890. [CrossRef]
5. Akishev, Y.; Grushin, M.; Napartovich, A.; Trushkin, N. Novel AC and DC non-thermal plasma sources for cold surface treatment of polymer films and fabrics at atmospheric pressure. *Plasmas Polym.* **2002**, *7*, 261–289. [CrossRef]
6. Neal, R.E., 2nd; Singh, R.; Hatcher, H.C.; Kock, N.D.; Torti, S.V.; Davalos, R.V. Treatment of breast cancer through the application of irreversible electroporation using a novel minimally invasive single needle electrode. *Breast Cancer Res. Treat.* **2010**, *123*, 295–301. [CrossRef]
7. Heller, L.C.; Jaroszeski, M.J.; Coppola, D.; McCray, A.N.; Hickey, J.; Heller, R. Optimization of cutaneous electrically mediated plasmid DNA delivery using novel electrode. *Gene Ther.* **2007**, *14*, 275–280. [CrossRef] [PubMed]
8. Zhang, S.; Jia, L.; Wang, W.-C.; Yang, D.-Z. Processes of Raising Voltage and Reducing Voltage in Needle-Plate Dielectric Barrier Discharge. *IEEE Trans. Plasma Sci.* **2013**, *41*, 2527–2531. [CrossRef]
9. He, H.; Xia, D.; Luo, B.; Chen, W.; Bian, K.; Xiang, N. Simulation of positive streamer propagation in an air gap with a GFRP composite barrier. *High Volt.* **2021**, *6*, 1079–1091. [CrossRef]
10. Tang, J.; Tang, M.; Zhou, D.; Kang, P.; Zhu, X.; Zhang, C. Hysteresis characteristics of the initiating and extinguishing boundaries in a nanosecond pulsed DBD. *Plasma Sci. Technol.* **2019**, *21*, 044001. [CrossRef]
11. Li, X.; Zhang, P.; Chu, J.; Zhang, Q.; Lin, X.; Jia, P.; Dong, L. Surface discharge induced interactions of filaments in argon dielectric barrier discharge at atmospheric pressure. *Phys. Plasmas* **2017**, *24*, 103520. [CrossRef]
12. Bruggeman, P.; Brandenburg, R. Atmospheric pressure discharge filaments and microplasmas: Physics, chemistry and diagnostics. *J. Phys. D Appl. Phys.* **2013**, *46*, 464001. [CrossRef]
13. Jidenko, N.; Petit, M.; Borra, J.P. Electrical characterization of microdischarges produced by dielectric barrier discharge in dry air at atmospheric pressure. *J. Phys. D Appl. Phys.* **2006**, *39*, 281–293. [CrossRef]
14. Laroussi, M.; Lu, X.; Kolobov, V.; Arslanbekov, R. Power consideration in the pulsed dielectric barrier discharge at atmospheric pressure. *J. Appl. Phys.* **2004**, *96*, 3028–3030. [CrossRef]

15. Sewraj, N.; Carman, R.J.; Merbahi, N.; Marchal, F.; Leyssenne, E. Spatiotemporal Distribution of a Monofilamentary Dielectric Barrier Discharge in Pure Nitrogen. *IEEE Trans. Plasma Sci.* **2011**, *39*, 2128–2129. [CrossRef]
16. Sewraj, N.; Merbahi, N.; Gardou, J.P.; Akerreta, P.R.; Marchal, F. Electric and spectroscopic analysis of a pure nitrogen monofilamentary dielectric barrier discharge (MF-DBD) at 760 Torr. *J. Phys. D Appl. Phys.* **2011**, *44*, 145201. [CrossRef]
17. Kozlov, K.V.; Wagner, H.E.; Brandenburg, R.; Michel, P. Spatio-temporally resolved spectroscopic diagnostics of the barrier discharge in air at atmospheric pressure. *J. Phys. D Appl. Phys.* **2001**, *34*, 3164–3176.
18. Brandenburg, R.; Wagner, H.E.; Morozov, A.M.; Kozlov, K.V. Axial and radial development of microdischarges of barrier discharges in N_2/O_2 mixtures at atmospheric pressure. *J. Phys. D Appl. Phys.* **2005**, *38*, 1649–1657. [CrossRef]
19. Yurgelenas, Y.V.; Wagner, H.E. A computational model of a barrier discharge in air at atmospheric pressure: The role of residual surface charges in microdischarge formation. *J. Phys. D Appl. Phys.* **2006**, *39*, 4031–4043.
20. Papageorghiou, L.; Panousis, E.; Loiseau, J.F.; Spyrou, N.; Held, B. Two-dimensional modelling of a nitrogen dielectric barrier discharge (DBD) at atmospheric pressure: Filament dynamics with the dielectric barrier on the cathode. *J. Phys. D Appl. Phys.* **2009**, *42*, 105201.
21. Becker, M.M.; Hoder, T.; Brandenburg, R.; Loffhagen, D. Analysis of microdischarges in asymmetric dielectric barrier discharges in argon. *J. Phys. D Appl. Phys.* **2013**, *46*, 355203. [CrossRef]
22. Babaeva, N.Y.; Kushner, M.J. Ion energy and angular distributions onto polymer surfaces delivered by dielectric barrier discharge filaments in air: I. Flat surfaces. *Plasma Sources Sci. Technol.* **2011**, *20*, 035017. [CrossRef]
23. Jovanovic, A.P.; Stankov, M.N.; Loffhagen, D.; Becker, M.M. Automated Fluid Model Generation and Numerical Analysis of Dielectric Barrier Discharges Using Comsol. *IEEE Trans. Plasma Sci.* **2021**, *49*, 3710–3718. [CrossRef]
24. Kettlitz, M.; Höft, H.; Hoder, T.; Reuter, S.; Weltmann, K.D.; Brandenburg, R. On the spatio-temporal development of pulsed barrier discharges: Influence of duty cycle variation. *J. Phys. D Appl. Phys.* **2012**, *45*, 245201. [CrossRef]
25. Kettlitz, M.; Höft, H.; Hoder, T.; Weltmann, K.D.; Brandenburg, R. Comparison of sinusoidal and pulsed-operated dielectric barrier discharges in an O_2/N_2 mixture at atmospheric pressure. *Plasma Sources Sci. Technol.* **2013**, *22*, 025003. [CrossRef]
26. Shao, T.; Zhang, C.; Yu, Y.; Niu, Z.; Jiang, H.; Xu, J.; Li, W.; Yan, P.; Zhou, Y. Discharge characteristic of nanosecond-pulse DBD in atmospheric air using magnetic compression pulsed power generator. *Vacuum* **2012**, *86*, 876–880. [CrossRef]
27. Yang, D.-Z.; Yang, Y.; Li, S.-Z.; Nie, D.-X.; Zhang, S.; Wang, W.-C. A homogeneous dielectric barrier discharge plasma excited by a bipolar nanosecond pulse in nitrogen and air. *Plasma Sources Sci. Technol.* **2012**, *21*, 035004. [CrossRef]
28. Liu, S.H.; Neiger, M. Excitation of dielectric barrier discharges by unipolar submicrosecond square pulses. *J. Phys. D-Appl. Phys.* **2001**, *34*, 1632–1638. [CrossRef]
29. Höft, H.; Becker, M.M.; Kettlitz, M. Correlation of axial and radial breakdown dynamics in dielectric barrier discharges. *Plasma Sources Sci. Technol.* **2018**, *27*, 03LT01. [CrossRef]
30. Höft, H.; Becker, M.M.; Loffhagen, D.; Kettlitz, M. On the influence of high voltage slope steepness on breakdown and development of pulsed dielectric barrier discharges. *Plasma Sources Sci. Technol.* **2016**, *25*, 064002. [CrossRef]
31. Kogelschatz, U. Collective phenomena in volume and surface barrier discharges. *J. Phys. Conf. Ser.* **2010**, *257*, 012015.
32. Gibalov, V.I.; Drimal, J.; Wronski, M.; Samoilovich, V.G. Barrier Discharge The Transferred Charge and Ozone Synthesis. *Contrib. Plasma Phys.* **1991**, *31*, 89–99. [CrossRef]
33. Ozkan, A.; Dufour, T.; Bogaerts, A.; Reniers, F. How do the barrier thickness and dielectric material influence the filamentary mode and CO_2 conversion in a flowing DBD? *Plasma Sources Sci. Technol.* **2016**, *25*, 045016. [CrossRef]
34. Meiners, A.; Leck, M.; Abel, B. Efficiency enhancement of a dielectric barrier plasma discharge by dielectric barrier optimization. *Rev. Sci. Instrum.* **2010**, *81*, 113507. [CrossRef]
35. Zhu, Y.; Shcherbanev, S.; Baron, B.; Starikovskaia, S. Nanosecond surface dielectric barrier discharge in atmospheric pressure air: I. measurements and 2D modeling of morphology, propagation and hydrodynamic perturbations. *Plasma Sources Sci. Technol.* **2017**, *26*, 125004. [CrossRef]
36. Zhu, Y.; Starikovskaia, S. Fast gas heating of nanosecond pulsed surface dielectric barrier discharge: Spatial distribution and fractional contribution from kinetics. *Plasma Sources Sci. Technol.* **2018**, *27*, 124007. [CrossRef]
37. Li, J.G. Upstream Nonoscillatory Advection Schemes. *Mon. Weather. Rev.* **2008**, *136*, 4709–4729. [CrossRef]
38. Verwer, J.G.; Sommeijer, B.P.; Hundsdorfer, W. RKC time-stepping for advection-diffusion-reaction problems. *J. Comput. Phys.* **2004**, *201*, 61–79.
39. Bourdon, A.; Pasko, V.P.; Liu, N.Y.; Célestin, S.; Ségur, P.; Marode, E. Efficient models for photoionization produced by non-thermal gas discharges in air based on radiative transfer and the Helmholtz equations. *Plasma Sources Sci. Technol.* **2007**, *16*, 656–678. [CrossRef]
40. Schenk, O.; Gartner, K. Solving unsymmetric sparse systems of linear equations with PARDISO. In *Computational Science—ICCS 2002 Proceedings Part II*; Sloot, P., Tan, C.J.K., Dongarra, J.J., Hoekstra, A.G., Eds.; Springer: Berlin/Heidelberg, Germany, 2002; Volume 2330, pp. 355–363.
41. Sonneveld, P. CGS, A Fast Lanczos-Type Solver For Nonsymmetric Linear-Systems. *Siam J. Sci. Stat. Comput.* **1989**, *10*, 36–52.

42. Ventzek, P.L.G.; Sommerer, T.J.; Hoekstra, R.J.; Kushner, M.J. 2-Dimensional Hybrid Model of Inductively-Coupled Plasma Sources for Etching. *Appl. Phys. Lett.* **1993**, *63*, 605–607. [CrossRef]
43. Villa, A.; Barbieri, L.; Gondola, M.; Malgesini, R. An asymptotic preserving scheme for the streamer simulation. *J. Comput. Phys.* **2013**, *242*, 86–102. [CrossRef]
44. Zhu, Y.; Chen, X.; Wu, Y.; Hao, J.; Ma, X.; Lu, P.; Tardiveau, P. Simulation of ionization-wave discharges: A direct comparison between the fluid model and E-FISH measurements. *Plasma Sources Sci. Technol.* **2021**, *30*, 075025. [CrossRef]
45. Phelps, A.V.; Pitchford, L.C. Anisotropic Scattering of Electrons by N_2 and Its Effect on Electron-Transport. *Phys. Rev. A* **1985**, *31*, 2932–2949. [CrossRef]
46. Lawton, S.A.; Phelps, A.V. Excitation of b $_1\sum^+_g$ State of O_2 by Low-Energy Electrons. *J. Chem. Phys.* **1978**, *69*, 1055–1068. [CrossRef]
47. Popov, N.A. Fast gas heating in a nitrogen-oxygen discharge plasma: I. Kinetic mechanism. *J. Phys. D-Appl. Phys.* **2011**, *44*, 285201. [CrossRef]
48. Pancheshnyi, S.; Nudnova, M.; Starikovskii, A. Development of a cathode-directed streamer discharge in air at different pressures: Experiment and comparison with direct numerical simulation. *Phys. Rev. E* **2005**, *71*, 016407. [CrossRef]
49. Kossyi, I.A.; Kostinsky, A.Y.; Matveyev, A.A.; Silakov, V.P. Kinetic scheme of the non-equilibrium discharge in nitrogen-oxygen mixtures. *Plasma Sources Sci. Technol.* **1992**, *1*, 207–220. [CrossRef]
50. Capitelli, M.; Ferreira, C.M.; Gordiets, B.F.; Osipov, A.I. *Plasma Kinetics in Atmospheric Gases*; Springer: Berlin/Heidelberg, Germany, 2001; Volume 31.
51. Zhang, Y.-T.; Wang, Y.-H. Modeling study on the effects of pulse rise rate in atmospheric pulsed discharges. *Phys. Plasmas* **2018**, *25*, 023509. [CrossRef]
52. Zouaghi, A.; Mekhaldi, A.; Gouri, R.; Zouzou, N. Analysis of nanosecond pulsed and square AC dielectric barrier discharges in planar configuration: Application to electrostatic precipitation. *IEEE Trans. Dielectr. Electr. Insul.* **2017**, *24*, 2314–2324. [CrossRef]
53. Jovanović, A.P.; Loffhagen, D.; Becker, M.M. Streamer–surface interaction in an atmospheric pressure dielectric barrier discharge in argon. *Plasma Sources Sci. Technol.* **2022**, *31*, 04LT02. [CrossRef]
54. Wang, Z.; Dijcks, S.; Guo, Y.H.; van der Leegte, M.; Sun, A.B.; Ebert, U.; Nijdam, S.; Teunissen, J. Quantitative modeling of streamer discharge branching in air. *Plasma Sources Sci. Technol.* **2023**, *32*, 085007. [CrossRef]

Disclaimer/Publisher's Note: The statements, opinions and data contained in all publications are solely those of the individual author(s) and contributor(s) and not of MDPI and/or the editor(s). MDPI and/or the editor(s) disclaim responsibility for any injury to people or property resulting from any ideas, methods, instructions or products referred to in the content.